Ceramics International 52 (2026) 42367–42381

Contents lists available at ScienceDirect

Ceramics International

journal homepage: www.elsevier.com/locate/ceramint

Role of lanthanum ions in modulating electrical conductivity and interfacial polarization behaviour in hard-soft $Co_{0.35}Mn_{0.35}Li_{0.15}Fe_{2.15-y}La_yO_4$ ferrite systems

Asad Nadeem [a,b], Iqra [a,*], Zeshan Munir [a], Salah Knani [c], Shahir Hussain [d], Nora Mobark Farhan [e], Le Duc Tung [f,g], Nguyen Thi Kim Thanh [f,g], Ohud Alzaidi [h], M.S. Al-Buriahi [i], Maria Akhtar [a,j,**], Muhammad Imran Arshad [a,***]

[a] Magnetic Interfaces & Materials Innovation (MIMI) Nanotech Research Lab, Department of Physics, Government College University, Faisalabad, Punjab, 38000, Pakistan
[b] Department of Physics, Division of Science and Technology, University of Education, Lahore, 54770, Pakistan
[c] Center for Scientific Research and Entrepreneurship, Northern Border University, Arar, 73213, Saudi Arabia
[d] Department of Electrical and Electronic Engineering, College of Engineering and Computer Science, Jazan University, PO Box. 706, Jazan, 45142, Saudi Arabia
[e] Department of Chemistry, College of Science, Princess Nourah bint Abdulrahman University, P.O. Box 84428, Riyadh, 11671, Saudi Arabia
[f] Biophysics Group, Department of Physics and Astronomy, University College London, Gower Street, London, WC1E 6BT, UK
[g] UCL Healthcare Biomagnetics and Nanomaterials Laboratories, 21 Albemarle Street, London, W1S 4BS, UK
[h] Department of Chemistry, College of Science - Al Khurma, Taif University, P.O. Box 11099, Taif, 21944, Saudi Arabia
[i] Department of Physics, Sakarya University, Sakarya, Turkey
[j] Center for High Energy Physics, University of the Punjab, Lahore, Pakistan

ARTICLE INFO

Keywords:
Sol-gel auto-combustion
Rare-earth doping
Spinel ferrites
Dielectric response
Functional materials

ABSTRACT

$Co_{0.35}Mn_{0.35}Li_{0.15}Fe_{2.15-y}La_yO_4$ (y = 0.00–0.05) were synthesized by using sol-gel auto-combustion method to investigate the effect of lanthanum substitution on the structural, optical, dielectric, electrical and magnetic properties. X-ray diffraction (XRD), the energy dispersive X-ray spectra (EDX), UV–visible spectroscopy, Raman spectroscopy, LCR, I–V analysis, and vibrating sample magnetometry (VSM) were performed to characterize the as-synthesized samples. XRD confirmed the predominantly cubic spinel structure with crystallite size ranging from 18.2 to 22.6 nm and lattice constant ranging from 8.38 to 8.47 Å and a weak $LaFeO_3$ secondary phase appeared at higher concentration of La^{3+} concentration. Additionally, the elemental analysis using EDX spectroscopy shows that the cations of cobalt, manganese, iron, and lanthanum are distributed uniformly, with no peaks seen for the cations of lithium ions because of their low atomic mass. UV–Visible analysis showed a systematic reduction in bandgap energy from 2.76 eV to 1.75 eV with increasing La^{3+} contents. Raman analysis revealed all the five characteristic spinel ferrite vibrational active modes with a peak shift after incorporation of La^{3+} ions. Dielectric properties were measured at room temperature over the frequency range of 4 Hz–8 MHz, showing a decline in dielectric constant and an increase in *ac* conductivity with the increasing lanthanum concentration. I–V analysis revealed an activation energy in the range of 0.52–1.05 eV. Magnetic measurements showed an initial increase in saturation magnetization to 156.16 emu/g for CML-0.01 followed by a decrease to 73.69 emu/g for CML-0.05 due to cation redistribution and magnetic dilution effects. The obtained results highlight the potential of the *Cu-Mn-Li* spinel ferrites specifically nanostructures of CML-0.04 and CML-0.05 for high frequency electronic applications.

* Corresponding author.
** Corresponding author. Center for High Energy Physics, University of the Punjab, Lahore Pakistan.
*** Corresponding author.
E-mail addresses: iqraranaphysicst@gmail.com (Iqra), saleh.kenani@nbu.edu.sa (S. Knani), dr.mariaakhtar11@yahoo.com (M. Akhtar), miarshad15@gmail.com (M.I. Arshad).

https://doi.org/10.1016/j.ceramint.2026.07.135
Received 29 April 2026; Received in revised form 16 June 2026; Accepted 8 July 2026
Available online 10 July 2026
0272-8842/© 2026 Elsevier Ltd and Techna Group S.r.l. All rights are reserved, including those for text and data mining, AI training, and similar technologies.

1. Introduction

The low coercivity, high magnetic permeability, electromagnetic properties, magnetization, and microwave absorption performance of multifunctional materials like ferrite-based composites make them highly promising for a wide range of diverse advanced applications. As a result, research on these materials is growing daily. Doping with rare earth metal ions can dramatically and effectively change their characteristics, leading to remarkably improved, adjustable, and distinctive multifunctional properties appropriate for a variety of advanced applications [1]. Due to their industrial significance and the fact that their cation distribution significantly affects their structural properties, spinel ferrites with the basic chemical formula AB_2O_4, where A and B stand for divalent and trivalent cations are of great interest [2]. Due to their broad and expanding technological relevance and extremely versatile functional characteristics, spinel ferrites have seen a significant increase in use in both technical and scientific fields in recent years, including memory devices, drug delivery systems, high-density storage media, gas sensors, super-capacitors, and transformer core applications [3]. Because of their remarkable and exceptional properties, such as magneto-crystalline anisotropy, high Curie temperature, relatively moderate saturation magnetization, high chemical stability, and electrical insulation properties that make them ideal for a variety of magnetic and electronic applications, cobalt ferrites ($CoFe_2O_4$) are hard ferrites that have been extensively studied [4]. Mn ferrites are the most prevalent type of soft ferrites and are highly useful for soft magnetic applications because of their relatively higher permeability, saturation magnetization, low magnetic loss, low power loss features, and coercivity values [5].

By changing the cation distribution and exchange interactions within the lattice, the substitution of rare earths (REs) into the spinel structure causes lattice distortion, structural deformation, and the introduction of internal microstrains that significantly and drastically change the magnetic and electrical behavior properties [6]. By adjusting the kinds and concentrations of metal ion dopants or substitution levels, the control of RE and metal ion substituents can successfully and efficiently modify the electromagnetic properties of nanocrystals (NCs), allowing for the fine-tuning of material performance aspects [7]. When RE cations are doped into the SFs, they are likely to occupy the octahedral (B) site, which lowers the chance of electron hopping and raises electrical resistance. Furthermore, controlled doping of RE cations (La^{3+}) into soft ferrites (SFs) can improve densification, permeability, and resistivity while optimizing magnetic and electrical performance and improving microstructural homogeneity [8]. Numerous studies have thoroughly studied the alteration of cation distribution in structural characteristics, magnetic behaviour, and electrical responsiveness of increasingly RE doped SFs, emphasising its important influence on the materials' overall multifunctional capabilities.

Khan, J.K. et al. [9] synthesized La^{3+} ions doped manganese-cobalt spinel ferrites and observed the crystallite size in the range of 9 nm - 14 nm range with highest impedance value for the $x = 0.15$ concentration. Khan, M. R. et al. [10] synthesized La^{3+} doped Cu-Co ferrites using sol-gel auto-combustion method and found the average particle size in the range of 27.9 nm - 40.9 nm, suitable for energy storage super capacitor applications. Ünal,B. et al. [11] synthesized La^{3+} doped Ni-Mn based soft ferrites using sol-gel auto-combustion method. They found crystallite size in the range of 10 nm - 15 nm with $x = 0.06$ sample showed most favourable dielectric properties governed by Maxwell-Wagner interfacial polarization. Arshad, M. I. et al. [12] synthesized La^{3+}-doped Co–Li–Ca ferrites using the sol-gel auto-combustion method and found the average nanoscale crystallite size of 11 nm and the bandgap energy of 3.25 eV for the $x = 0.03$ La concentration level. Ul Haq et al. [13] investigated the impact of Ce^{3+} and La^{3+} co-doping on the structural, optical, and electrical properties of Mg-Zn spinel ferrites nanostructures. This co-doping has been demonstrated to significantly improve the material system's overall dielectric performance and stability, leading to a notable and significant increase in impedance and a decrease in dielectric loss.

The current study's intentional use of the sol-gel auto-combustion method aims to support circular economy models in materials manufacturing through cost-effective and environmentally sustainable processing strategies by utilizing energy-efficient synthetic routes that offer high scalability and minimal waste generation in comparison to traditional solid-state reaction methods. The sol–gel auto-combustion process is a self-propagating and self-sustaining way of generating heat energy through its exothermic processes. It offers a number of beneficial features, including improved distribution, decreased particle size, enhanced compositional uniformity, and controlled morphology at the nanoscale level, all of which contribute to superior material properties. A quick, economical, and energy-efficient synthetic technique for creating particulate materials with regulated nanostructures and enhanced homogeneity is sol-gel auto-combustion method. By mixing elements at the atomic level, it has been widely utilized to synthesize various nanoparticles and produce Nano-sized, homogenous, and highly reactive powders [14]. For advanced application fields, this enables increased material reactivity and accurate and fine compositional control. Under comparatively low external energy input circumstances, sol-gel auto-combustion method is a self-sustaining process that produces heat through its exothermic reaction, allowing for rapid and accelerated crystallisation and phase formation processes [15].

Spinel ferrites containing cobalt, manganese, and lithium ions have attracted increasing attention because the presence of these cations provide a unique combination of structural stability, magnetic anisotropy, electrical conductivity, and dielectric polarization. Moreover, the addition of rare-earth ions leads to modified crystal structure, better charge transport mechanism and magnetic exchange interactions due to their larger ionic radius. To the best of our knowledge, this is the first work on lanthanum-doped compositions of $Co_{0.35}Mn_{0.35}Li_{0.15}Fe_{2.15-y}La_yO_4$ ferrites, where y varies as 0.0, 0.01, 0.02, 0.03, 0.04, and 0.05 mol fraction levels [CML-0.00, CML-0.01, CML-0.02, CML-0.03, CML-0.04, and CML-0.05], synthesized by using the sol-gel auto-combustion method. This article discusses the systematic and thorough effects of lanthanum ions on the structural, optical, electrical, and magnetic properties of *Co–Mn–Li* ferrite nanostructures.

2. Experiment and characterizations

2.1. Materials and synthesis route

The series of $Co_{0.35}Mn_{0.35}Li_{0.15}Fe_{2.15}yLa_yO_4$ ferrites, where $y = 0.00$, 0.01, 0.02, 0.03, 0.04, and 0.05, were prepared by using the sol–gel auto-combustion method. The chemicals $Co(NO_3)_2{\cdot}6H_2O$, $MnCl_2{\cdot}4H_2O$, $Fe(NO_3)_3{\cdot}9H_2O$, $LiNO_3$, and $La(NO_3)_3{\cdot}6H_2O$, were dissolved in distilled water according to their stoichiometric calculations and continuously stirred on a magnetic stirrer in a beaker at 353 K for 2 h. A separate beaker with a magnetic stirrer was used to properly prepare a solution of citric acid ($C_6H_8O_7$) in distilled water with a metal ion to citric acid molar ratio of 1:1. After thoroughly mixing all of the nitrate solutions, ammonia was added dropwise until pH 7 was reached, citric acid was added, and the mixture was constantly stirred. The solution was then heated to form viscous gel, followed by self-combustion to produce fluffy ash. The ash was ground to a fine powder and the powder was sintered at 973 K for 9 h in an oxidizing atmosphere in a muffle furnace using a heating rate of 5 K min^{-1}. After sintering, the samples were furnace-cooled naturally to room temperature and were again ground to a fine powder. The powder was then used to make pellets of approximately 2 mm diameter by using a hydraulic press to measure the dielectric and electrical properties of the samples. The synthetic route used for the CML-0.00, CML-0.01, CML-0.02, CML-0.03, CML-0.04, and CML-0.05 ferrites preparation is shown in Fig. 1.

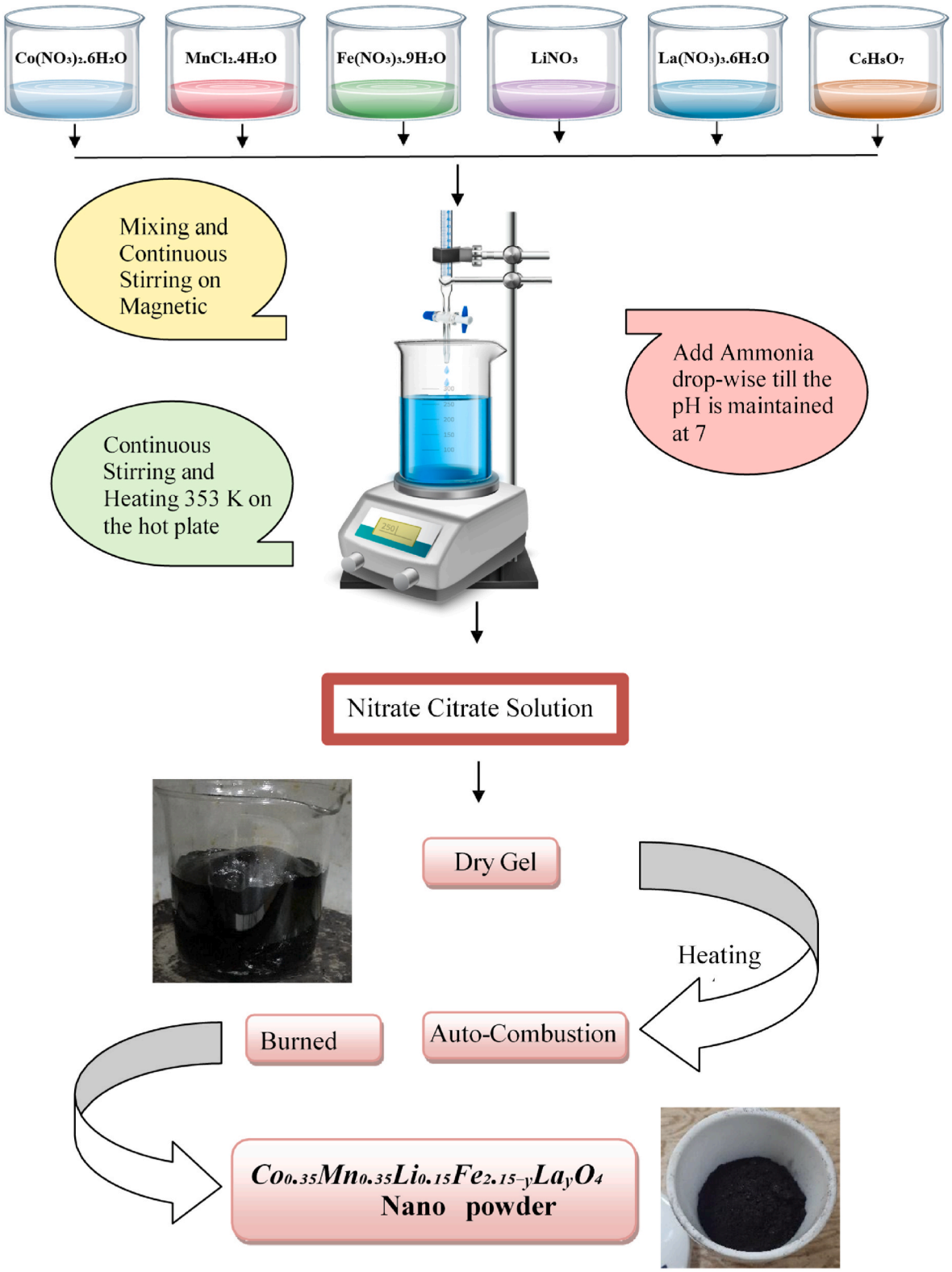


Fig. 1. Synthesis route for the CML-0.00, CML-0.01, CML-0.02, CML-0.03, CML-0.04, and CML-0.05 spinel ferrites sintered at 973 K for 9 h.

2.2. Characterization techniques

Several common and sophisticated characterization techniques were used to describe the prepared samples. To find the Bragg angle (2θ) inside the 20°–60° scanning window, XRD was carried out using radiations from a filtered CuKα source with wavelength λ = 1.5417 Å using a Bruker X-ray diffractometer, Model D8 Advance. Crystallite size, X-ray density, bulk density, lattice constant, packing fraction, porosity, strain, and unit cell volume and surface area were among the many XRD properties that were carefully and painstakingly determined. The energy dispersive X-ray spectra were used to analyze the stoichiometry of the produced samples (EDX). Two probes were used to assess DC resistivity

using a Keithley Model 2401 Source-meter IV measurement (current, voltage, resistance measure meter). The commercial spectrometer LABRAM-HR was used to record Raman spectra. UV visible spectroscopy was performed by UV-DS, Model Lamda 25 for obtaining band gap energy. An IM3533 series LCR metre and impedance analyzer (IA) were used to measure dielectric in the broad spectral window of 4 Hz to 8 MHz.

3. Results and discussion

3.1. Structural analysis

XRD analysis of the CML-0.00, CML-0.01, CML-0.02, CML-0.03, CML-0.04, and CML-0.05 samples is shown in Fig. 2. The observed peaks are indexed as (220) at 30.01°, (311) at 35.13°, (400) at 42.84°, and (511) at 56.66°. The most intense peak was observed at 35.13° with the Miller index (311). The extra peak at $2\theta = 44.65°$ corresponds to the secondary phase of $LaFeO_3$ and matches literature reports [16]. This secondary phase does not match the cubic spinel phase structure and is caused by trace levels of $LaFeO_3$ at the specimen's borders. It shows the La^{3+} ions' solubility limit and incorporation threshold in the spinel ferrites system's cubic lattice [17]. Bragg's law, which is expressed as follows, can be used to compute the interplanar distance dhkl.

$$d_{hkl} = \frac{n\lambda}{2\sin\theta} \tag{1}$$

where $n = 1$ is the order of reflection, $\lambda = 1.5417$ Å is the wavelength, and θ is the Bragg angle.

The lattice parameters of the prepared sample were calculated using the following formula

$$A = d_{hkl}\left[h^2 + k^2 + l^2\right]^{1/2} \tag{2}$$

where d is the interplanar (inter-layer spacing) distance between crystallographic planes and (h k l) are Miller indices.

The crystallite size (D), which is provided by the following expression/equation, was determined using Scherrer's formula.

$$D = \frac{k\lambda}{\beta\cos\theta} \tag{3}$$

Where D represents the crystallite size, $k = 0.98$ is the shape factor of the material and is a dimensionless quantity, λ represents the wavelength of radiations used, β is the full width half maxima (FWHM), and θ is the Bragg angle [18].

It was observed from Table 1 that the lattice constant increases as the doping concentration of La^{3+} increases up to $y = 0.03$, and then decreases [19]. This characteristic is caused by the complete and efficient incorporation of lanthanum ions into the spinel lattice structure at low concentrations. Lattice expansion takes place because the ionic radius of La^{3+} is relatively and significantly larger than that of the Fe^{3+} ions they replace, which increases the value of the lattice constant. However, some lanthanum cations have a tendency to disperse and migrate to the grain boundaries during sintering, creating a thin, isolated intergranular layer around the grains. At higher doping concentrations, less lanthanum enters the sublattice, while more accumulates at the grain boundaries. This grain-boundary $LaFeO_3$ phase exerts an extrusion stress on the crystal lattice. As the lanthanum concentration increases further, the stress from the grain-boundary impurities becomes greater than the internal stress from lanthanum in the lattice, causing the lattice constant to decrease, reaching a minimum at high doping levels [20]. Similarly, up to $y = 0.03$, the crystallite size (D) decreased with increasing La^{3+} concentration before increasing as a result of changes in the lattice constant. Variations are also seen in the X-ray density, as shown in Table 1. This variation is attributed to the presence of unavoidable pores that form during synthesis and sintering.

The following formula was used for the calculation of X-ray density.

$$d_{x-ray} = \frac{ZM}{a^3 N_A} \tag{4}$$

where $Z = 8$ for the spinel cubic structure, N_A is Avogadro's number ($6.022 \times 10^{23}\ mol^{-1}$), M is the molecular weight, and a is the lattice parameter.

Bulk density d_b was calculated using the following formula:

$$d_b = \frac{m}{\pi r^2 h} \tag{5}$$

In this case, h stands for the pellet's thickness and r for its radius. It was discovered that changes in sample mass had an impact on the bulk density, which is very mass-dependent.

The porosity (p%) was calculated using the formula,

$$p\% = 1 - \frac{d_b}{d_x} \tag{6}$$

Where d_b is the bulk density and d_x is the x-ray density.

Unit cell volume and packing fraction were calculated using formula

$$\text{Unit cell volume} = V = a^3 \tag{7}$$

Where a is the lattice constant.

The packing fraction (P) provides information about the compactness of the material and was calculated as:

$$\text{Packing fraction } (P) = \frac{D}{d_{hkl}} \tag{8}$$

Where D represents the crystallite size of the synthesized samples and d_{hkl} is the inter-planer distance.

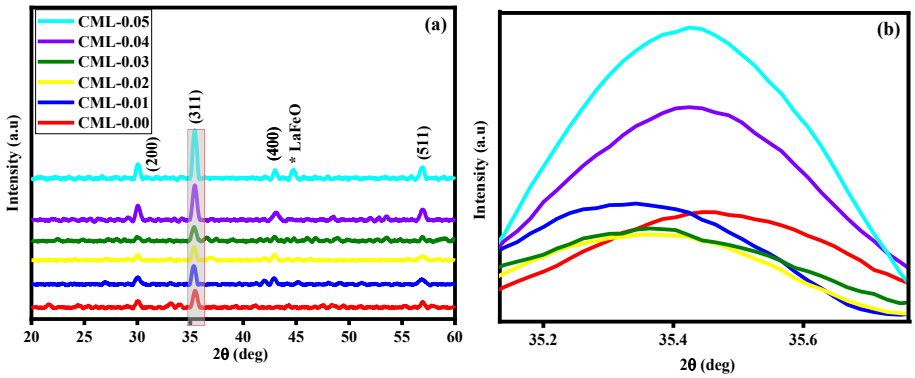


Fig. 2. (a) Powder XRD patterns of CML-0.00, CML-0.01, CML-0.02, CML-0.03, CML-0.04, and CML-0.05 spinel ferrites, and **(b)** magnified view of the 311 peak from 35.2 to 36.6°.

Table 1
Calculated XRD parameters for CML-0.00, CML-0.01, CML-0.02, CML-0.03, CML-0.04, and CML-0.05 ferrites.

Parameters	Samples					
	CML-0.00	CML-0.01	CML-0.02	CML-0.03	CML-0.04	CML0.05
a (Å)	8.38	8.40	8.40	8.47	8.45	8.39
d (Å)	2.52	2.53	2.53	2.55	2.54	2.53
D (nm)	19.6	18.8	18.7	18.2	18.3	22.5
d_X (gcm^{-3})	5.07	5.03	5.07	4.96	5.02	5.15
V $(Å)^3$	589.45 64.5%	595.48 64.55%	593.85 64.5%	608.15 64.03%	604.18 66.1%	590.82 67.4%
p%	64.5%	64.55%	64.5%	64.03%	66.1%	67.4%
Strain (ε)	0.156	0.155	0.155	0.153	0.153	0.156
P	77.72	88.92	74.23	71.38	71.68	89.30
S (m^2/g)	60.21	52.79	62.89	66.20	65.40	51.53
d_b (gcm^{-3})	1.78	1.79	1.80	1.82	1.72	1.68
Rwp	45	62	69	54	48	33
Rexp	31	40	47	36	29	22
χ2	1.45	1.55	1.47	1.50	1.66	1.50

Strain represents the lattice distortions present within the crystal lattice and calculated using formula

$$\text{Strain} = \mathscr{E} = \frac{\beta}{4\ tan\ \theta} \tag{9}$$

Where d_{hkl} is inter-planner distance, and surface area was calculated as:

$$\text{Surface area} = S = \frac{6000}{d_x} * D \tag{10}$$

Where d_x is x-ray density and D is crystallite size.

According to Table 1, the bulk density first increased with increasing La^{3+} doping concentration up to y = 0.03 before progressively declining. The reason for this variance is that lanthanum ions have a substantially higher atomic mass than iron ions. All samples had bulk densities ranging from 1.68 to 1.82 g/cm^3 and X-ray densities ranging from 4.96 to 5.15 g/cm^3. The porosity (p%) also shows variation, as it is defined as the ratio of bulk density to X-ray density; thus, changes in density values lead to corresponding changes in porosity. Porosity (p%) exhibits a nonlinear trend with increasing lanthanum content. Other parameters, including specific surface area S, strain Ɛ, unit cell volume V, and packing fraction P, were also calculated and are listed in Table 1 and are shown in Fig. 3. Rietveld refinement XRD patterns of CML-0.00, CML-0.01, CML-0.02, CML-0.03, CML-0.04, and CML-0.05 spinel ferrites are shown in Fig. 4, obtained by using FULLPROF program. Several R-factors, such as the weighted profile factor (Rwp), expected factor (Rexp), and goodness-of-fit ($\chi^2 = \frac{Rwp}{Rexp}$), which is frequently used to evaluate the

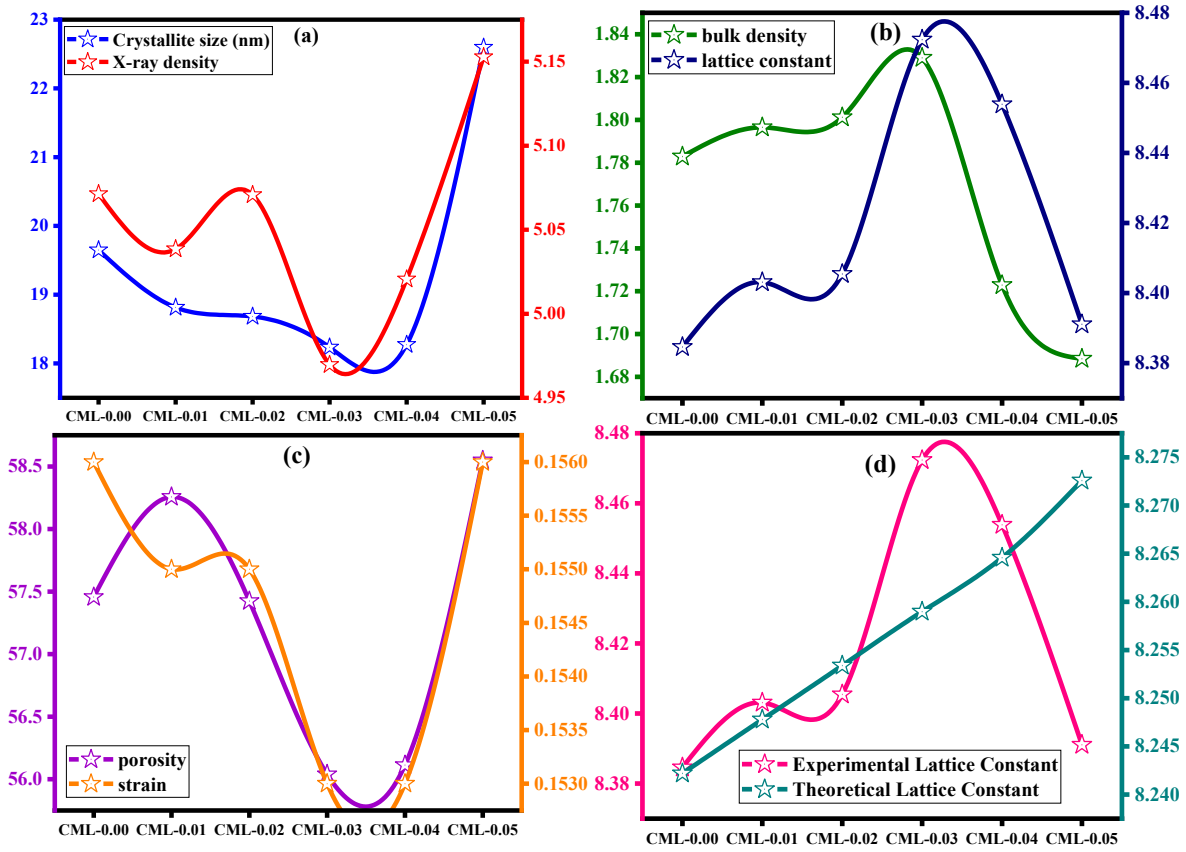


Fig. 3. Calculated XRD parameters: **(a)** crystallite size and X-ray density, **(b)** bulk density and lattice constant, **(c)** porosity and strain, and **(d)** experimental and theoretical lattice constant for CML-0.00, CML-0.01, CML-0.02, CML-0.03, CML-0.04, and CML-0.05 spinel ferrites.

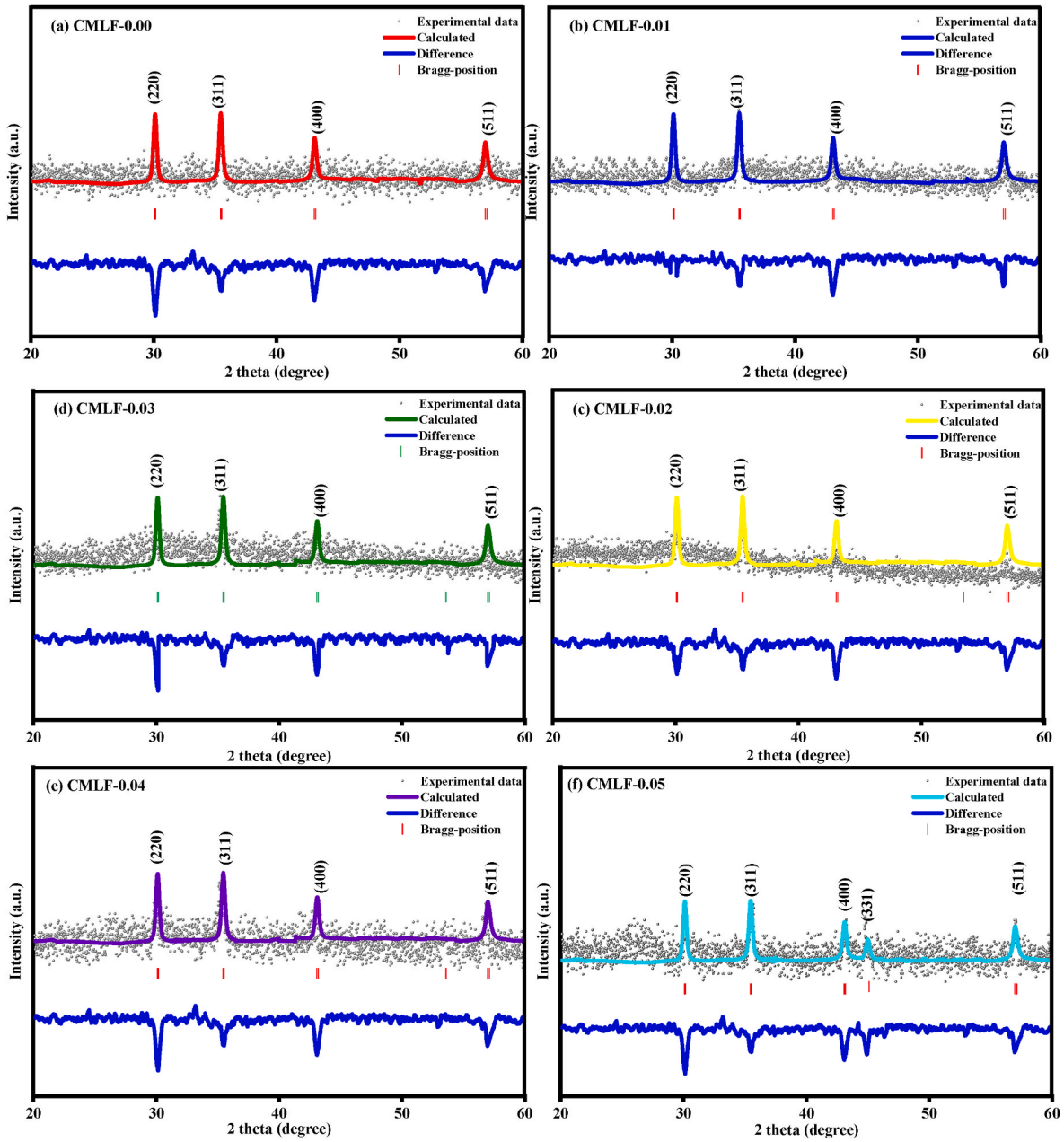


Fig. 4. (a–f) Rietveld refinement patterns of CML-0.00, CML-0.01, CML-0.02, CML-0.03, CML-0.04, and CML-0.05 spinel ferrites.

quality of the fitting process, are utilized to measure the reliability of the refinement. Table 1 summarizes the revised parameters determined from the Rietveld refinement study.

3.2. Cation distribution

Equations (11) and (12) were used to get the ionic radii r_A(Å) and r_B(Å). Table 2 listed the cationic radii of Co, Mn, Li, Fe, and La, while

Table 2
The cationic radii of Co, Mn, Li, Fe, and La ions.

Elements	A-site (%)	B-site (%)	r_A (Å)	r_B (Å)
Co	20	80	0.58	0.74
Mn	5	95	0.66	0.83
Li	10	90	0.74	0.90
Fe	22.5	77.5	0.49	0.64
La	-	-	-	1.06

Table 3
Cationic distribution estimated for CML-0.00, CML-0.01, CML-0.02, CML-0.03, CML-0.04, and CML-0.05 using XRD analysis.

Samples	Tetrahedral site	Octahedral site
CML-0.00	$[Co_{0.07}Mn_{0.0175}Li_{0.015}Fe_{0.4837}]$ A	$[Co_{0.28}Mn_{0.3325}Li_{0.135}Fe_{1.6662}La_{0}]$ BO_4
CML-0.01	$[Co_{0.07}Mn_{0.0175}Li_{0.015}Fe_{0.4837}]$ A	$[Co_{0.28}Mn_{0.3325}Li_{0.135}Fe_{1.6562}La_{0.01}]$ BO_4
CML-0.02	$[Co_{0.07}Mn_{0.0175}Li_{0.015}Fe_{0.4837}]$ A	$[Co_{0.28}Mn_{0.3325}Li_{0.135}Fe_{1.6462}La_{0.02}]$ BO_4
CML-0.03	$[Co_{0.07}Mn_{0.0175}Li_{0.015}Fe_{0.4837}]$ A	$[Co_{0.28}Mn_{0.3325}Li_{0.135}Fe_{1.6362}La_{0.03}]$ BO_4
CML-0.04	$[Co_{0.07}Mn_{0.0175}Li_{0.015}Fe_{0.4837}]$ A	$[Co_{0.28}Mn_{0.3325}Li_{0.135}Fe_{1.6262}La_{0.04}]$ BO_4
CML-0.05	$[Co_{0.07}Mn_{0.0175}Li_{0.015}Fe_{0.4837}]$ A	$[Co_{0.28}Mn_{0.3325}Li_{0.135}Fe_{1.6162}La_{0.05}]$ BO_4

Table 3 listed a potential cationic distribution.

$$r_A = C_{ACo}r(Co^{2+}) + C_{AMn}r(Mn^{2+}) + C_{ALi}r(Li^{1+}) + C_{AFe}r(Fe^{2+}) \quad (11)$$

$$r_A = \frac{1}{2}\left[C_{ACo}r(Co^{2+}) + C_{AMn}r(Mn^{2+}) + C_{ALi}r(Li^{1+}) + C_{AFe}r(Fe^{2+}) + C_{ALa}r(La^{2+})\right] \quad (12)$$

Because lanthanum ions do not occupy the tetrahedral site, Table 4 demonstrated that the values of r_A (Å) can stay constant, whereas the values of r_B (Å) progressively increase as a result of the incorporation of La^{3+} ions into the octahedral site, which has an ionic radius of 1.06° greater than that of Fe^{3+} ions (0.64°).

Equation (13) provided the relationship that was used to derive the theoretical lattice constant. $a_{th} = \frac{8}{\sqrt{3}}\left[(r_A + R_0) + \sqrt{3}(r_B + R_0)\right]$ **(13)**

Here, R_0 is the oxygen ion radius, which is equal to 1.32 Å, while r_A and r_B stand for the ionic radius at tetrahedral and octahedral sites, respectively.

Table 4 displays the computed values of a th, which exhibit a systematic and progressive increasing trend as a result of the doping of a dopant element with a greater ionic radius than the local iron ion radius (Fe^{3+}). The tolerance factor (T) was calculated using the relation shown in equation (14).

$$T = \frac{1}{\sqrt{3}}\left(\frac{r_A + R_0}{r_B + R_0}\right) + \frac{1}{\sqrt{2}}\left(\frac{R_0}{r_A + R_0}\right) \quad (14)$$

The spinel structure is confirmed using the tolerance factor (T), which is equal to 1 for an ideal spinel. The small deviation of the tolerance factor from unity (as shown in Table 4) is attributed to the incorporation of La^{3+} ions, which slightly distort the spinel structure.

The oxygen positional parameter (U) was calculated using relation 15.

$$U = (r_A + R_0)\frac{1}{\sqrt{3}a} + \frac{1}{4} \quad (15)$$

From the literature, the standard value of the oxygen positional parameter (u) is 0.375 Å. The slight deviation in the observed values (see Table 4) is attributed to the anion displacement caused by the incorporation of La^{3+} ions [21]. The variation in the experimental lattice constant at high doping concentrations is attributed to charge accumulation at the grain boundaries and the solubility limit of La^{3+} ions in the spinel structure.

3.3. EDX analysis

EDX was utilized to confirm elemental composition of the $Co_{0.35}Mn_{0.35}Li_{0.15}Fe_{2.15-y}La_yO_4$ nanoparticles (where y = 0.00-0.05) and the EDX pattern is shown in Fig. 5. The presence of Co, Mn, Fe, O, and La was confirmed by the peaks, indicating that La^{3+} had been successfully substituted in cobalt-manganese ferrites. This proves that no integrated components were tainted or lost. Due to its low atomic number (Z), which is less than the sensitivity of EDX, the element lithium (Li) is actually invisible in the spectrum [22]. The observed Li-ion ratio is evidently almost constant and closely matches the necessary chemical formula [23]. The following relation was used to compute the number of moles of each element from EDX data [24].

$$\text{No of moles (Me)} = \frac{\text{Observed wt\% (Me)} \times \text{molecular wt of sample}}{\text{atomic wt of (Me)} \times 100}$$

The calculated numerical quantities for EDX analysis are given in Table 5. Samples with the required composition have been synthesized, even if the measured values from EDX and the anticipated values of the elements are not comparable. The concentration of Fe decreased when the La content was added to the CMLF-0.05 sample. The EDX examination of weight % of elements indicates that the samples have the required compositions and that the required elements are present in the required ratio.

Table 4
Different XRD parameters of CML-0.00, CML-0.01, CML-0.02, CML-0.03, CML-0.04, and CML-0.05 ferrites.

Samples	r_A (Å)	r_B (Å)	a_{th} (Å)	U (Å)	T
CML-0.00	0.3002	0.8354	8.2422	0.3635	1.0100
CML-0.01	0.3002	0.8375	8.2478	0.3634	1.0097
CML-0.02	0.3002	0.8396	8.2590	0.3634	1.00924
CML-0.03	0.3002	0.8417	8.2560	0.3633	1.0088
CML-0.04	0.3002	0.8438	8.2646	0.3632	1.0084
CML-0.05	0.3002	0.8468	8.2726	0.3631	1.0078

3.4. Optical properties

Solution of CML-0.00, CML-0.01, CML-0.02, CML-0.03, CML-0.04, and CML-0.05 ferrites in de-ionized water was made for obtaining UV-Vis spectra. In this process, non-bonding electrons are stimulated by UV-light by giving them energy, and these electrons subsequently interact with anti-bonding electrons in excited states. The band gap energy value was calculated using the Tauc relation

$$\alpha h\upsilon = (h\upsilon - Eg)^m \quad (16)$$

Here hυ is the photons energy hitting the targeted sample, α is the absorption coefficient, Eg is the optical bandgap energy, and m has values 1/2 or 2 depending upon the gap between valence and conduction band. Indirect permissible transitions have m = 2, while direct allowed transitions have m = 1/2. The direct transition model (m = 1/2) was used in this investigation based on earlier results for spinel ferrites.

Absorption coefficient α was calculated as

$$\alpha = \frac{(2.303)log(A)}{t} \quad (17)$$

Here t is 1 cm showing cuvette's width.

A material's optical bandgap is frequently influenced by a number of factors, including grain size, dopant concentration, lattice structure parameters, lattice strain, surface effects, and the presence of structural and chemical impurities inside the lattice system [25]. As the concentration of La^{3+} increased, a decrease in the bandgap energy is observed, which could lead to defect formation, lattice deformation, and localized states. The larger ionic radius of La^{3+} influence the optical absorption behavior, loosening the bonding of the outermost electrons, requiring less energy to remove them from the crystal lattice. The direct bandgap energy was found to range from 2.76 to 1.75 eV, as shown in Fig. 6 and listed in Table 6 while the indirect bandgap energy value was ranged between 2.92 eV and 1.23 eV shown in Fig. 7 and listed in Table 6. The bandgap energy, which is inversely related to the La^{3+} doping concentration, is trending downward in the corresponding graph. The direct and indirect bandgap energy (Eg) dropped as the bonding strength of the outermost electrons decreased with increasing La^{3+} content [26]. Although both direct and indirect bandgaps have reasonable energy values, the direct bandgap plots exhibited a more reliable extrapolation to the energy axis.

3.5. Raman analysis

The Raman spectra of the synthesized samples exhibited five peaks in the range of 200–750 cm^{-1}, corresponding to the presence of five different cations in the structure, as shown in Fig. 8 and Table 7. The force constants linked to the vibrations of the corresponding cations in the unit cell and are shown by the sub-peaks that were created from each peak.

The symmetric stretching of the (Fe/M)–O bond is represented by A_1g in the Raman spectra, whereas the equivalent asymmetric (antisymmetric) stretching is represented by $T_{2g}(2)$. $T_2g(3)$ represents anti-

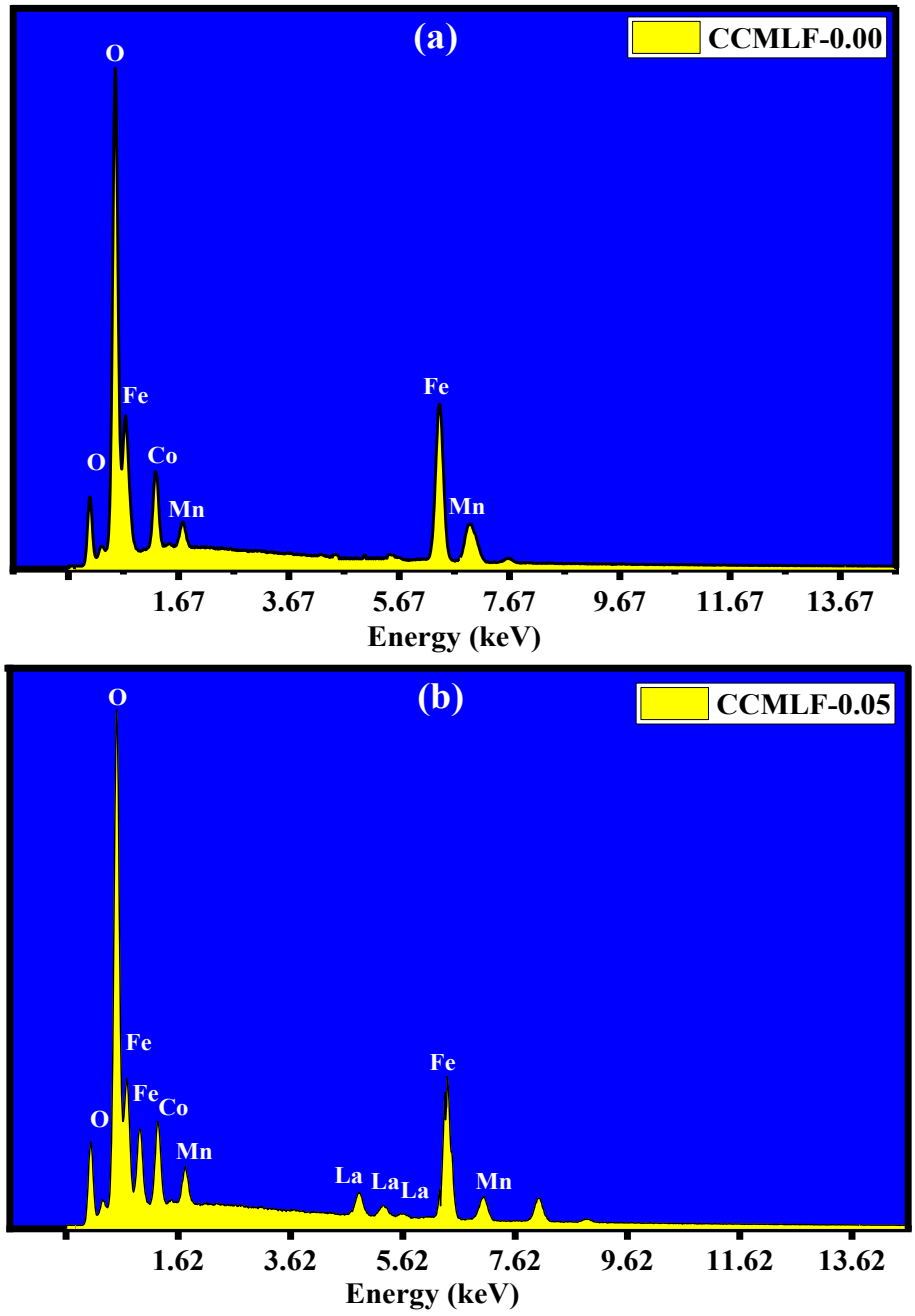


Fig. 5. EDX spectra for La-substituted CMLF-0.00 and CMLF-0.05 samples.

Table 5
Calculated EDX parameters of CML-0.00, CML-0.01, CML-0.02, CML-0.03, CML-0.04, and CML-0.05 ferrites.

Samples	Formula	Elements	Atomic wt%	Weight % (Expected)	Weight % (Experimental)	% error
CMLF-0.00	$Co_{0.35}Mn_{0.35}Li_{0.15}Fe_{2.15}O_4$	Co	5.00	9.17	8.88	3.16
		Mn	5.00	8.55	7.79	8.89
		Fe	30.71	53.37	52.30	2.00
		La	0.00	0.00	0.00	0.00
		O	57.14	28.45	27.98	1.65
CMLF-0.05	$Co_{0.35}Mn_{0.35}Li_{0.15}Fe_{2.10}La_{0.05}O_4$	Co	5.00	9.00	8.97	0.33
		Mn	5.00	8.39	8.32	0.83
		Fe	30.00	51.19	51.06	0.25
		La	0.71	3.03	2.78	8.25
		O	57.14	27.93	27.80	0.47

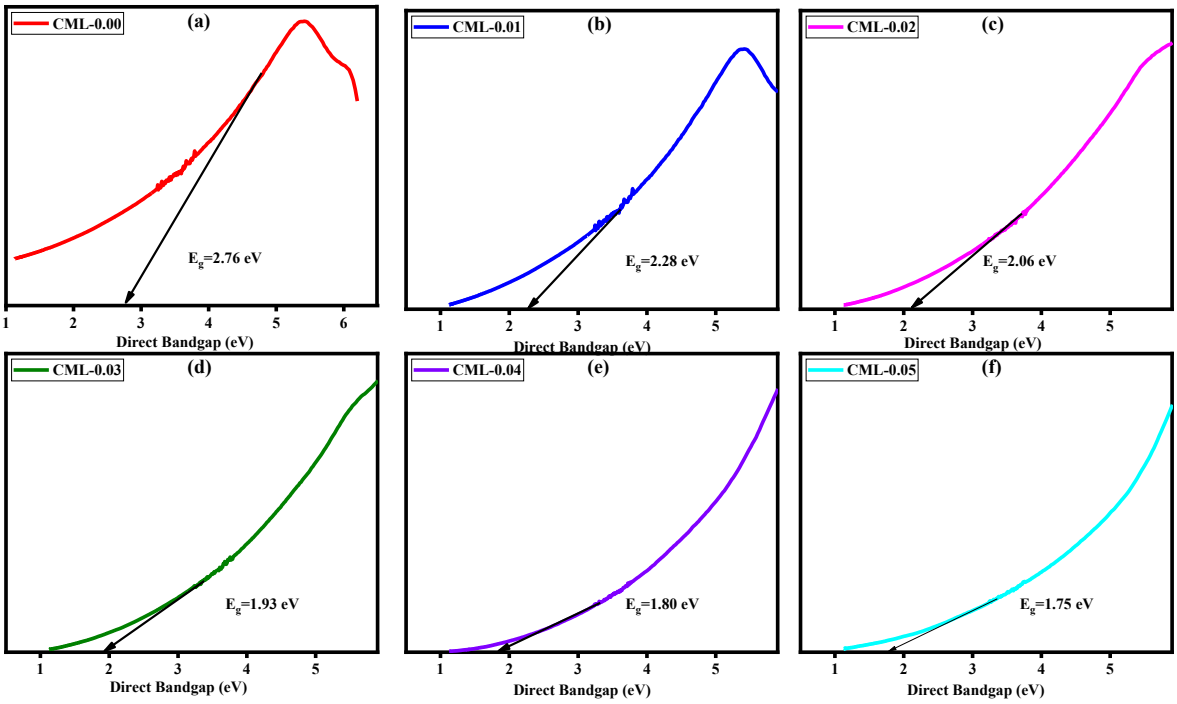


Fig. 6. Direct energy bandgap values of CML-0.00, CML-0.01, CML-0.02, CML-0.03, CML-0.04, and CML-0.05 ferrites.

Table 6
Energy band gap values of CML-0.00, CML-0.01, CML-0.02, CML-0.03, CML-0.04, and CML-0.05 ferrites.

Samples	Direct bandgap Energy E_g (eV)	Indirect bandgap Energy E_g (eV)
CML-0.00	2.76	2.93
CML-0.01	2.28	2.83
CML-0.02	2.06	2.85
CML-0.03	1.93	2.58
CML-0.04	1.80	2.86
CML-0.05	1.75	1.23

symmetric vibrational modes, while Eg represents anti-symmetric Fe–O bond bending vibrations. Since each peak in these five Raman modes is characteristic of the spinel lattice structure, the spinel structure is confirmed. The disruption and modification of cation distributions in the spinel structure caused by lanthanum doping is confirmed by peak position shifts and intensity variations (power adjustments) in Raman spectra concerning bond length, electronegativity, and stability of vibrational modes at octahedral and tetrahedral sites of the vibrating species [27]. The substitutional incorporation of La^{3+} ions and the resulting lattice distortion resulted in progressive broadening of Raman bands with increasing La^{3+} concentration, which indicates an incease in structural disorder and microstrain inside the crystal lattice.

3.6. Dielectric analysis

The dielectric properties of La^{3+} doped series of CML-0.00, CML-0.01, CML-0.02, CML-0.03, CML-0.04, and CML-0.05 were studied using LCR technique under the frequency range of 4Hz to 8 MHz. Fig. 9(a) illustrates how the dielectric constant (ε') varies with log(frequency). The graph displays a slow and steady dropping trend in ε' with increasing La^{3+} doping concentration, indicating that the dielectric constant steadily decreased as the doping level increased, consistent with the literature [28]. The decrease in ε' with frequency in soft ferrite systems is caused by the polarization mechanisms according to which at low frequencies, charge carrier hopping is simple and leads to higher dielectric value responses and at higher frequencies, hopping is more complex and constrained, leading to a decrease in the dielectric constant value. Furthermore, polarization is changed by charge accumulation at grain boundaries as a result of La^{3+} incorporation. Sintering temperature, grain size, stoichiometry, synthetic process, cation ratio, and oxygen parameter are some of the other parameters that affect the dielectric constant [29]. The addition of La^{3+} ions results in a decreasing trend in dielectric loss when frequency shifts from 4 Hz to 8 MHz, demonstrating an inverse relationship between frequency and dielectric loss.

The dielectric constant (ε') and dielectric loss (tanδe) graphs clearly showed that both show high values at low frequencies and drop with increasing frequency, which is typical for ferrites [30]. However, dielectric loss (ε'') decreased rapidly with increasing frequency, whereas the dielectric constant shows a more gradual decrease and becomes nearly frequency-independent at high frequencies, consistent with literature reports [31], as shown in Fig. 9(b).

Dielectric tangent loss (tanδe) is the ratio of dielectric loss to the dielectric constant, which measures the electrical energy loss as heat when an external electric field is applied to the prepared samples at different frequencies.

$$\text{Tan } \delta e = \frac{\textit{dielectric loss}}{\textit{dielectric constant}} \tag{18}$$

It was found that the dielectric tangent loss decreased with frequency at room temperature and has high values at low frequency, shown in Fig. 10(a). At low frequencies, conducting grains are more visible than comparatively thinner grain boundaries, which resulted in a significant dielectric tangent loss (tanδe). The Q-factor provides the connection between stored energy and the rate of energy dissipation in electrical device systems. As a result, the nonlinear trend represents the normal and unique behaviour of ferrites as reported in the literature, and Q-factor values offer useful information about the manufactured La^{3+} doped samples [32]. The variation in Q-factor with log(f) is shown in Fig. 10(b) clearly. The graph showed that the value of Q-factor increased by adding La^{3+} ions concentration in each sample such that varies as y from 0 to 0.05.

AC conductivity was calculated using relation

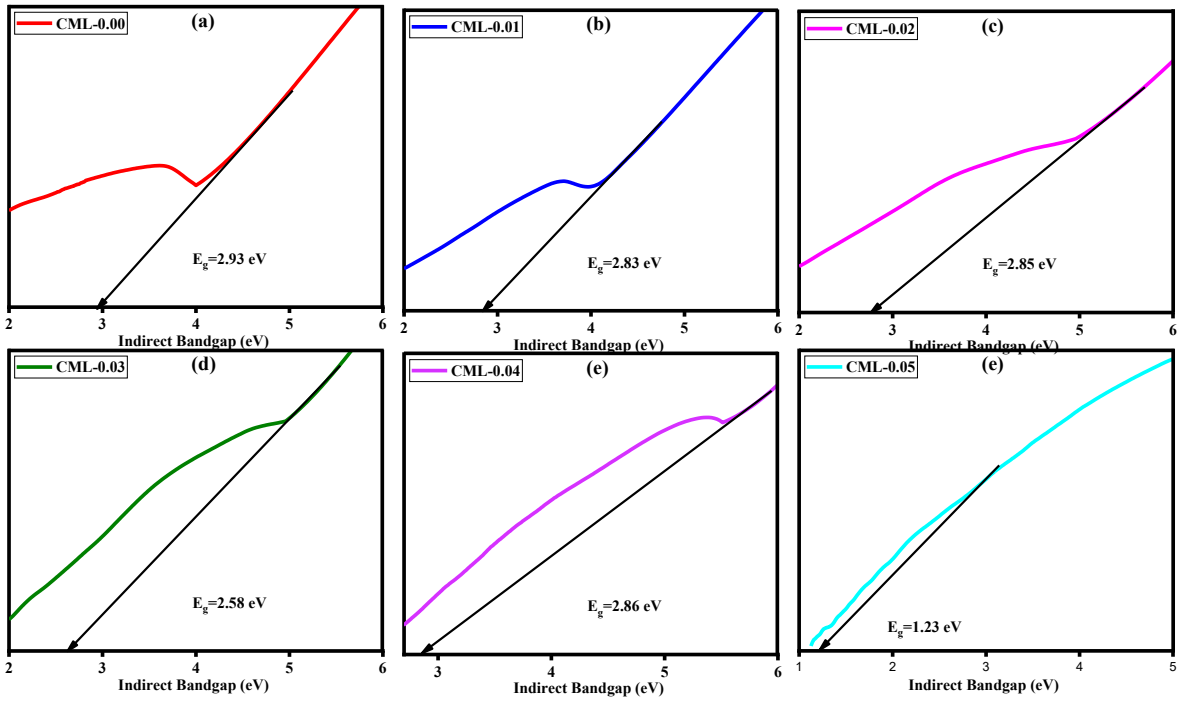


Fig. 7. Indirect energy bandgap values of CML-0.00, CML-0.01, CML-0.02, CML-0.03, CML-0.04, and CML-0.05 ferrites.

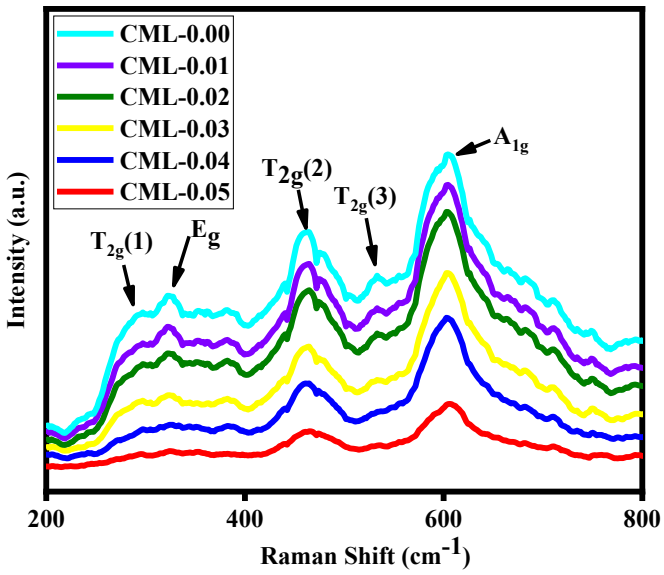


Fig. 8. Relationship between Intensity and Raman shift of CML-0.00, CML-0.01, CML-0.02, CML-0.03, CML-0.04, and CML-0.05 ferrites.

Table 7
Raman absorption peaks for different La^{3+} doping concentrations.

Parameters	Samples					
	CML-0.00	CML-0.01	CML-0.02	CML-0.03	CML-0.04	CML0.05
$T_{2g}(1)$	295	294	292	293	294	294
E_g	315	313	310	314	316	315
$T_{2g}(2)$	480	480	481	483	483	482
$T_{2g}(3)$	532	532	530	532	532	531
A_{1g}	608	607	609	610	608	608

$$\sigma_{ac} = 2\pi f \times \tan \delta e \quad (19)$$

A direct correlation between frequency and ac conductivity was shown in the accompanying graph. The hopping electrons of the same elements with several valence states are what give ferrites their conductivity. According to Koop's theory, grain boundaries are more active at low frequencies, which prevents electrons from moving freely. As a result, hopping is reduced and low *ac* conductivity is observed at low frequencies. They show a relatively high value of permittivity at low frequencies, where the grain boundary impact is more apparent, because the thickness of the barrier layer (formed by charge accumulation at grain boundaries following the addition of La^{3+} ions) and capacitance have an inverse relationship, i.e., $C \propto 1/d$ (where d is thickness). High frequencies cause an increase in grain activity, which promotes electron hopping between Fe^{2+} and Fe^{3+} cations and actively aids in the formation of new charge carriers. This behaviour boosts *ac* conductivity and decreases obstacles to charge mobility, which is consistent with the literature [33]. The change in the impedance with respect to frequency is shown in Fig. 11(a). The impedance value steadily drops as the frequency increases, indicates an increase in *ac* conductivity. In Fig. 11(b), the impedance vs. frequency plot gives an indication of an increase in conduction with frequency, which infers that the ferrites behave like a semiconducting material [34].

3.7. I-V analysis

Current-voltage measurements were taken for the study of the electrical properties of the prepared samples shown in Fig. 12. A hydraulic press was used to create the pellets, and silver paste was applied to the disk-shaped pellets to facilitate conduction. Electrical characteristics like DC resistivity were computed at various temperatures, ranging from ambient temperature to 400 K, using the two-probe method. DC resistivity was calculated using the formula:

$$\rho = \frac{RA}{L} \quad (20)$$

where ρ, A, R, and L represents the resistivity, area of pellet, resistance, and thickness of pellet, respectively.

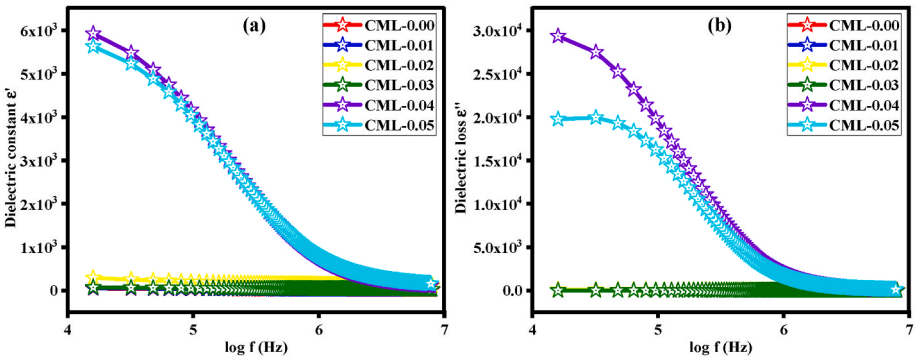


Fig. 9. The dependence between **(a)** dielectric constant and log of frequency, and **(b)** dielectric loss and log of frequency.

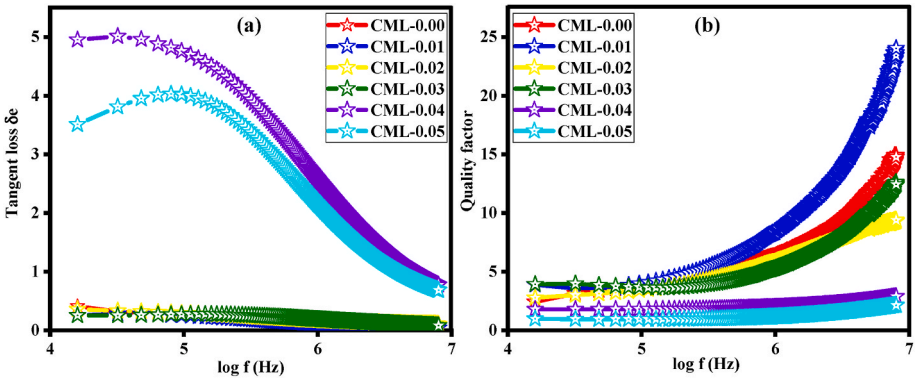


Fig. 10. The dependence between **(a)** dielectric tangent loss and log of frequency, and **(b)** quality factor and log of frequency.

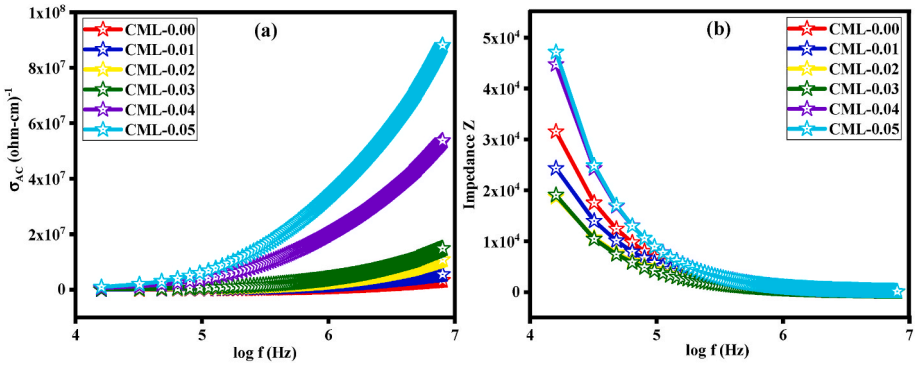


Fig. 11. The dependence between **(a)** ac conductivity and log of frequency, and **(b)** impedance and log of frequency.

Fig. 13 showed a decrease in the value of resistivity when doping concentration is increased, with a minimum value at y = 0.04. This is due to the replacement of La^{3+} ions with Fe^{3+} ions at the octahedral site. Also, the logarithm of resistivity decreases as temperature increases. Charge hopping is caused by various electron transfer channels, such as Fe^{3+}–Me and Fe^{2+}–Fe^{3+} in the produced nano-ferrites. Electrical properties were systematically changed as a result of the partial replacement of RE cations for Fe^{3+}, which results in lattice distortion, structural deformation, and internal strain in the spinel matrix framework [35]. At octahedral (B) sites, La^{3+} cations exhibit a high preferred occupancy. Consequently, the mobility and concentration of charge carriers increased, leading to enhanced electrical conductivity [36]. The Arrhenius plots (log ρ vs 1000/T) for La^{3+} doped Co–Mn–Li nano-ferrite are shown in Fig. 13. Fig. 13 has two regions, the first region starts from 305 to 345 K and the second region from 345 K to above, in between them there is transition temperature. Before the transition temperature, the region is ferromagnetic; beyond that, it changes into a paramagnetic phase. The activation energy Ea, of the prepared nanoparticles is calculated using:

$$E_a = 2.303 \times k_B \times 10^3 \times \text{slope (eV)} \quad (21)$$

Here k_B is the Boltzmann constant. The activation energy (Ea = Ep − Ef) [37] is calculated and listed in Table 8. The activation energy first decreased and then increased and decreased in the later end shown in Fig. 14.

3.8. Magnetic analysis

The La^{3+}-substituted CML-0.00, CML-0.01, CML-0.02, CML-0.03, CML-0.04, and CML-0.05 samples' hysteresis loops (M − H loops) with a comparatively low coercive field are clearly displayed in Fig. 15. The computed magnetic parameters for each sample under investigation are

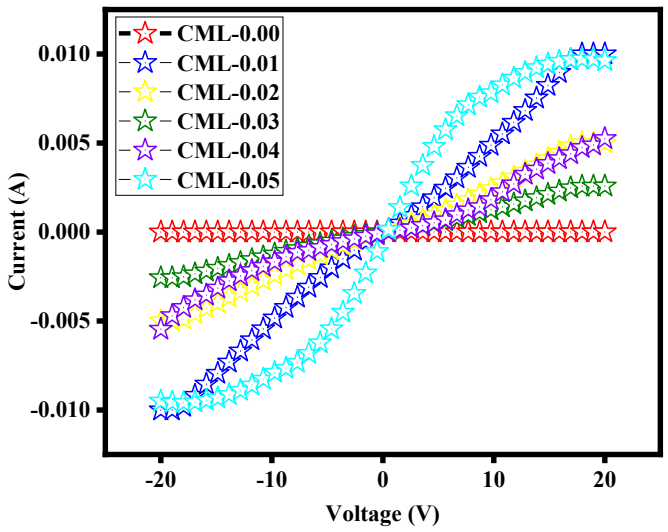


Fig. 12. The dependence between current and voltage at room temperature.

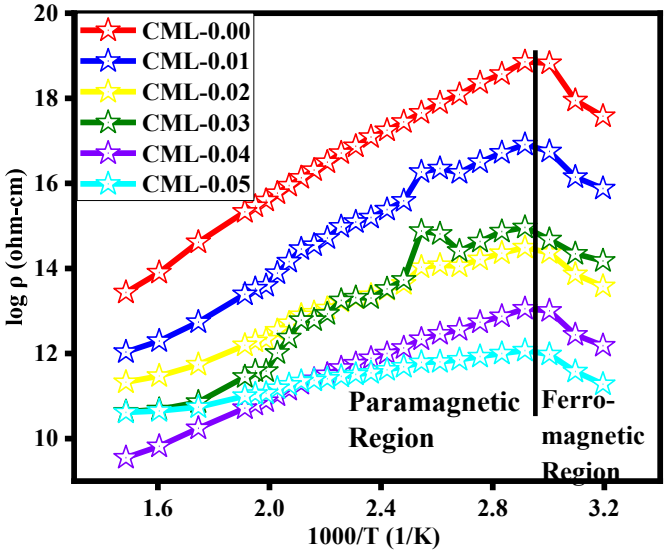


Fig. 13. The dependence between the log of resistivity and 1000/T.

Table 8
Calculated values of activation energy.

Samples	Tc (K)	E_p	E_f	$E_a = E_p$-E_f
CML-0.00	341	0.70	−0.30	1.00
CML-0.01	345	0.65	−0.28	0.93
CML-0.02	342	0.43	−0.26	0.69
CML-0.03	343	0.69	−0.36	1.05
CML-0.04	336	0.64	−0.29	0.91
CML-0.05	338	0.24	−0.28	0.52

shown in Table 9. The CML-0.01 sample displayed maximum saturation magnetization (M_S) of 156.16 emu/g and remanent magnetization (Mr) of 40.49 emu/g, whereas the CML-0.05 sample displayed minimum Ms of 73.69 emu/g and remanent magnetization of 12.41 emu/g. This might be due to the CMLF spinel lattice structure's substitution of nonmagnetic La^{3+} ions replacing Fe^{3+} ions. In addition, small amounts of lanthanum could lead to decrease in spin canting, stronger magnetic ordering and reduced surface spin disorder. These effects may have resulted in temporarily outweigh the magnetic dilution caused by La ions and resulted in increased Ms value at initial incorporation.

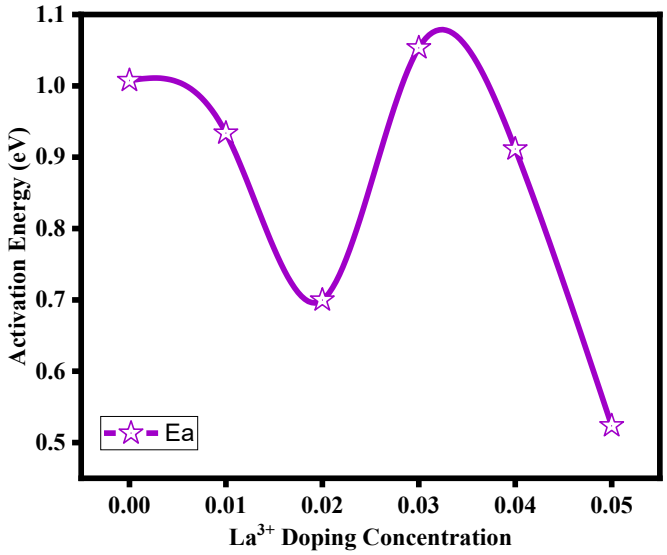


Fig. 14. The dependence between activation energy and La^{3+} doping concentration.

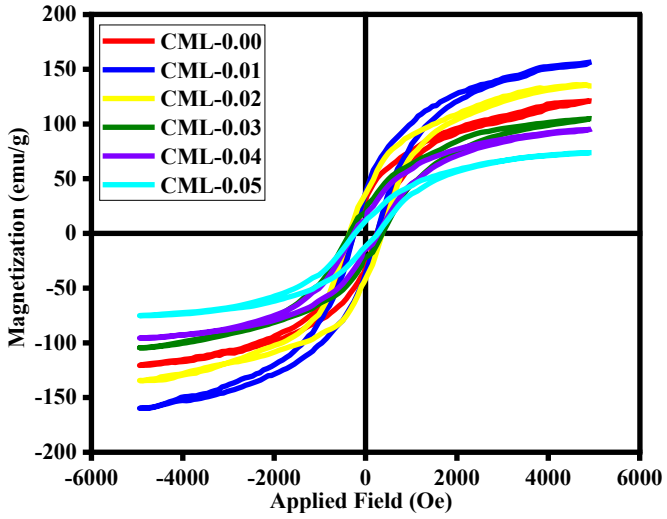


Fig. 15. M – H loops of the as-synthesized CML-0.00, CML-0.01, CML-0.02, CML-0.03, CML-0.04, and CML-0.05 ferrites with varying La^{3+} concentration.

Following that, Ms progressively decreased as the La^{3+} doping concentration increased, reaching 73.69 emu/g for the CML-0.05 sample. A–B interactions between magnetic sublattices, particle size, and cation distribution all have a significant impact on the magnetic properties of the SFs [38–41]. The notable increase in M_S for x = 0.01 is caused by the rearrangement and redistribution of cations inside the A- and B-sites of the spinel lattice. The effect of substituting non-magnetic La^{3+} for Fe^{3+} (5 μB), the prominent primary contributor to the magnetic characteristics at the B-site of the SFs, may be explained by the much reduced and weakened A–O–B super-exchange interaction mechanism. The cation content at the A- and B-sites inside the crystal lattice framework is known to have a major impact on the magnetic characteristics of SFs with the AB_2O_4 spinel crystal matrix system. Exchange interactions between A–A and B–B sites form AB_2O_4, whereas superexchange interactions are represented by (A–B). Compared to the (A–A) and (B–B) interactions, the (A–B) interaction shows significantly stronger and more dominant magnetic coupling interactions inside the spinel system. Due to the occupancy of La^{3+} ions, the concentration of Fe^{3+} ions at the SFs' B-site systematically decreased. This reduced the (B–B) contacts

Table 9
Calculated magnetic values of CML-0.00, CML-0.01, CML-0.02, CML-0.03, CML-0.04, and CML-0.05 samples.

Samples	Calculated Parameters							
	Ms	Mr	Hc	Sq	μi	μ_B	ω_m	K
CML-0.00	120.9	33.6	232	0.2779	9.82	4.86	2.66×10^{10}	29210
CML-0.01	156.2	40.5	233	0.2593	12.12	6.31	3.44×10^{10}	37820
CML-0.02	134.6	37.8	388	0.2809	6.22	5.46	2.97×10^{10}	54417
CML-0.03	104.5	20.2	387	0.1933	4.72	4.25	2.30×10^{10}	42127
CML-0.04	95.54	13.4	311	0.1407	5.39	3.90	2.11×10^{10}	30901
CML-0.05	73.69	12.4	229	0.1684	6.99	3.02	1.62×10^{10}	17540

and, consequently, the (A–B) super-exchange interactions across sub-lattices across the crystal lattice. Stated differently, the B-site magnetic behaviour in SFs lattices is mostly caused by the strongly magnetic Fe^{3+} (5 μB) ions. The B–B (Fe^{3+}–Fe^{3+}) interactions steadily reduced when non-magnetic La^{3+} ions eventually replaced magnetic Fe^{3+} ions. Therefore, a comparable and overall drop in the net magnetic moment can be linked to a decrease in the magnetic moment with increased La^{3+} doping [42,43]. The sample CML-0.05 had a minimum coercivity of 228.5 Oe, while the maximum coercivity (HC) for CML-0.02 was 388 Oe. At low La concentrations, the increase in strain and local lattice distortion may enhance domain-wall pinning, leading to higher Hc, whereas at higher La concentrations the combined effects of magnetic dilution and structural modifications facilitate domain-wall motion, resulting in reduced coercivity. The materials' soft magnetic nature is indicated by their low coercivity values, which are advantageous for dielectric and magnetic properties [44]. Although Brown's relation predicts an inverse dependence of coercivity on saturation magnetization, this relationship is not always strictly followed in nanocrystalline ferrites because coercivity is also influenced by crystallite size, lattice strain, magnetocrystalline anisotropy, and domain-wall pinning. The simultaneous increase in Ms and Hc observed for the CML-0.01 sample may be attributed to improved magnetic ordering and reduced spin canting, which enhance Ms, together with increased lattice distortion and strain that strengthen domain-wall pinning and increase Hc. Grain size, surface effects, and the movement of domain walls within the material microstructure are some of the significant extrinsic factors that affect the coercivity behaviour. Lastly, the doping of the La^{3+} ion into the lattice with the Fe^{3+} ion may be the cause of the change in magnetic

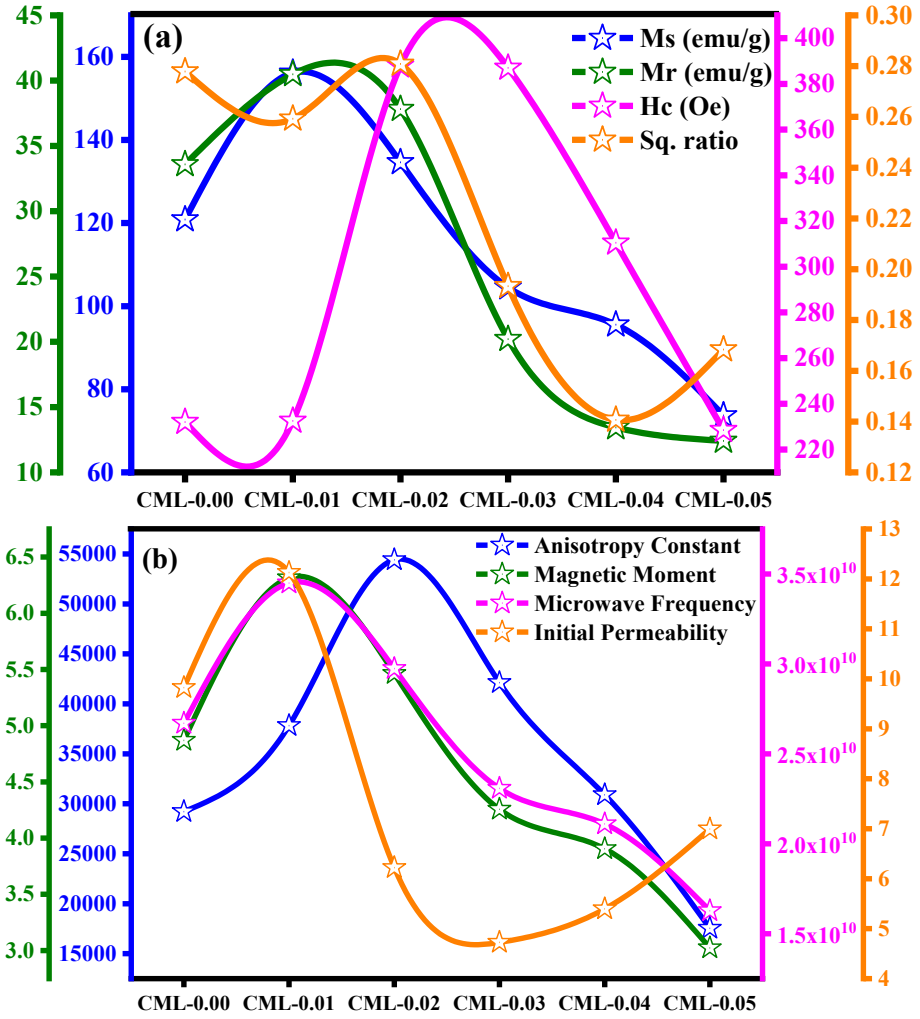


Fig. 16. Calculated magnetic parameters of the as-synthesized CML-0.00, CML-0.01, CML-0.02, CML-0.03, CML-0.04, and CML-0.05 ferrites with varying La^{3+} concentration.

properties. This could affect the Fe^{3+} ion's magnetic moment alignment, which alters and systematically rearranges the Fe^{3+} ion arrangement inside the crystal structure framework. The soft magnetic characteristics of CML-0.00, CML-0.01, CML-0.02, CML-0.03, CML-0.04, and CML-0.05 samples were gradually and methodically changed by La^{3+} doping, making them appropriate for high-frequency applications including inductor cores, circulators, and high-frequency electronic devices devices. As shown in Table 9, the squareness ratio (Sq = Mr/Ms) significantly and constantly dropped with increasing La^{3+} content; for the CML-0.04 sample in particular, the minimum Sq was found to be 0.14. Particle magneto-static interaction effects are represented by the value of "Sq," which is less than 0.5. As a result, the Sq ratio for each of the CML-0.00, CML-0.01, CML-0.02, CML-0.03, CML-0.04, and CML-0.05 samples demonstrated the particle contact controlled by magnetostatic interaction between nearby grains/particles. The anisotropy constant (K) was calculated by $K = \frac{M_s \times H_c}{0.96}$ and the value of "K" is affected by both Ms and Hc parameters. Initial permeability was calculated by $\mu_i = \frac{M_s^2 \times D}{K}$, where K is the magnetic anisotropy constant, D is the crystallite size, and Ms is the saturation magnetization. The magnetic moment was calculated by using the formula $\mu_B = \frac{M_w \times M_s}{5585}$ and found in the range of 3.02–6.31 μ_B, as shown in Fig. 16 [45]. Due to its strong dependence on saturation magnetization, the magnetic moment shows a similar and constant pattern [46]. The microwave operating frequency was calculated using $\omega_m = 8\pi^2 M s \gamma$ (where $\gamma = 2.8$ MHz/Oe is the gyromagnetic ratio) [47], and values of "ω_m" were found to be in the gigahertz range as seen in Table 9. The microwave frequency response characteristic of CML-0.00, CML-0.01, CML-0.02, CML-0.03, CML-0.04, and CML-0.05 samples makes them a good option for high-frequency based applications.

4. Conclusion

Lanthanum-doped *Co-Mn-Li* soft ferrites were synthesized via the sol-gel route. Characterization was performed using XRD, Raman, UV–Vis, LCR, and IV techniques. The predominantly cubic spinel structure was confirmed by XRD data, and the intense peaks of each sample appeared at an average angle of 35.28° with Miller indices (311) with a minor peak of $LaFO_3$ was observed for CML-0.05 sample. XRD analysis was used to calculate lattice characteristics, including bulk density, X-ray density, crystallite size, lattice constant, and others. Furthermore, EDX proved a homogeneous distribution of cobalt, manganese, iron and lanthanum cations with no peaks observed for lithium cations. Raman shifts varied with La^{3+} doping, as confirmed by Raman data. UV–Vis study showed the band gap energy decreasing from 2.76 to 1.75 eV. DC resistivity, obtained from IV analysis, showed a decreasing trend with increasing temperature. LCR measurements provided information about dielectric constant, dielectric loss, and *ac* conductivity trends with frequency. AC conductivity increased with increasing frequency. Overall, the results indicate that the prepared ferrite samples exhibit semiconducting-like behavior. La^{3+} substitution in the spinel lattice systematically reduces saturation magnetization and coercivity while maintaining soft magnetic behavior potentially suitable for future high-frequency electronic applications.

CRediT authorship contribution statement

Asad Nadeem: Writing – original draft. **Iqra:** Software, Writing – review & editing. **Zeshan Munir:** Formal analysis. **Salah Knani:** Visualization. **Shahir Hussain:** Data curation. **Nora Mobark Farhan:** Funding acquisition. **Le Duc Tung:** Writing – review & editing. **Nguyen Thi Kim Thanh:** Writing – review & editing. **Ohud Alzaidi:** Resources. **M.S. Al-Buriahi:** Validation. **Maria Akhtar:** Methodology. **Muhammad Imran Arshad:** Conceptualization, Supervision.

Declaration of competing interest

The authors declare that they have no known competing financial interests or personal relationships that could have appeared to influence the work reported in this paper.

Acknowledgement

The authors express their gratitude to Princess Nourah bint Abdulrahman University Researchers Supporting Project number (PNURSP2026R963), Princess Nourah bint Abdulrahman University, Riyadh, Saudi Arabia. The authors extend their appreciation to the Deanship of Scientific Research at Northern Border University, Arar, KSA for funding this research work through the project number "NBU-CRP-2026-2483"

References

[1] A. Baykal, B.A.Y. Ünal, M.A. Almessiere, A.D. Korkmaz, Y. Slimani, Role of La/Ce co-substitution in modulating conductivity and interfacial polarization in hard-soft CoFe2O4/NiFe2O4 spinel ferrite nanocomposites [H/S CoLaxCexFe2-2xO4/NiFe2O4 (x≤ 0.10) SFNCs], Appl. Phys. A 132 (3) (2026) 231, https://doi.org/10.1007/s00339-026-09421-5.

[2] Y. Abbas, M. Kamran, H. Mazhar, M. Anis-ur-Rehman, Correlation of Structure and Transport Properties of Bi2Ca2− x La x CoO6 Nanoparticles Synthesized by Coprecipitation Method: Y. Abbas et al, J. Electron. Mater. 54 (11) (2025) 9700–9713, https://doi.org/10.1016/j.jallcom.2025.180340.

[3] A. Alhadhrami, M. Zeshan, H.M.T. Farid, The structural and dielectric properties of lanthanum substituted strontium based spinel ferrites nano-materials for high frequency device applications, J. Taibah Univ. Sci. 17 (1) (2023) 2236368, https://doi.org/10.1080/16583655.2023.2236368.

[4] H.G. Abd-Elbaky, M. Rasly, R.G. Deghadi, G.G. Mohamed, M.M. Rashad, Strong-base free synthesis enhancing the structural, magnetic and optical properties of Mn/Co and Zn/Co substituted cobalt ferrites, J. Mater. Res. Technol. 20 (2022) 905–915, https://doi.org/10.1016/j.jmrt.2022.07.106.

[5] M.S. Hossen, R.S. Auntu, A. Debnath, S.K. Shil, Structural, morphological, electromagnetic, and dielectric properties of solid state method synthesized co-mn-zn nano ferrites, Ceram. Int. (2025), https://doi.org/10.1016/j.ceramint.2025.07.102.

[6] O. Manner, S. Sarmah, K.P. Patra, D. Maji, S. Ravi, T. Bora, Effect of rare earth (Ho and Er) co-substitution on the magnetic and dielectric properties of nanocrystalline cobalt ferrites, Ceram. Int. 50 (17) (2024) 30912–30930, https://doi.org/10.1016/j.ceramint.2024.05.397.

[7] M.A. Abbasi, M. Khalid, W. Ullah, M.G.B. Ashiq, M. Younas, Structural, morphological, dielectric and magnetic properties of La3+ ion doped Zn–Mg based spinel ferrites nanomaterials for technological applications, Ceram. Int. (2026), https://doi.org/10.1016/j.ceramint.2026.05.024.

[8] G. Maragathavalli, S. Mugundan, T. Sivasakthi, B. Askaribanu, C.P. Reddy, Impact of lanthanum (La) incorporation on the xylene gas detection capabilities of zinc ferrite ($ZnFe_2O_4$) nanoparticles, Inorg. Chem. Commun. (2025) 115330, https://doi.org/10.1016/j.inoche.2025.115330.

[9] J.K. Khan, M. Khalid, G. Mustafa, Z. Uddin, M. Saleem, A.A. Azam, Study of lanthanum ions (La3+) doped manganese-cobalt (Mn-Co) based spinel ferrite nanoparticles for technological applications, Appl. Phys. A 128 (11) (2022) 961, https://doi.org/10.1007/s00339-022-06106-7.

[10] M.R. Khan, H. Mahajan, A.K. Srivastava, Investigation of crystallographic, morphological, magnetic and electrochemical properties of la-doped Cu-CoFe2O4 spinel ferrites, Cryst. Res. Technol. 59 (7) (2024) 2300356, https://doi.org/10.1002/crat.202300356.

[11] B.A.Y. Ünal, M.A. Almessiere, A. Baykal, A.D. Korkmaz, M.A. Gondal, S.E. Shirsath, Y. Slimani, Correlating microstructure and electrical properties: the role of lanthanum doping in Mn-Ni nanospinel ferrites, Mater. Chem. Phys. (2025) 131929, https://doi.org/10.1016/j.matchemphys.2025.131929.

[12] M.I. Arshad, A. Dastgir, F. Alresheedi, N. Amin, L.D. Tung, M. Amami, A. U. Rehman, Electrically and magneto-dielectrically modified La3+ doped Co0.3Li0.1Ca0.5Fe2.1-xLaxO4 spinel ferrites and their potential applications, J. Alloys Compd. 978 (2024) 173015, https://doi.org/10.1016/j.jallcom.2023.173015.

[13] M.I.U. Haq, A.U. Rehman, M. Asghar, M.A.U. Nabi, N. Amin, S. Tahir, M.I. Arshad, Influence of Ce3+ and La3+ substitution on structural & optical parameters and electrical behavior on Mg-Zn ferrites synthesized via co-precipitation method, J. Supercond. Nov. Magnetism 35 (3) (2022) 719–732, https://doi.org/10.1007/s10948-021-06124-1.

[14] S. Roostaei, H. Ansarinejad, E.A. Dawi, F.H. Alsultany, S.K. Issa, M. Ahmadi-Kashani, M. Salavati-Niasari, Sol–gel auto-combustion synthesis of a novel ternary magnetic-recyclable ZnFe2O4/ZnO/CeO2 nano-photocatalyst for highly efficient visible-light-induced degradation of organic contaminants, Appl. Water Sci. 15 (8) (2025) 193, https://doi.org/10.1007/s13201-025-02549-4.

[15] S.P. Sahare, A.V. Wankhade, A.K. Sinha, S.P. Zodape, Modified cobalt ferrite entrapped chitosan beads as a magnetic adsorbent for effective removal of malachite green and copper (II) ions from aqueous solutions, J. Inorg. Organomet.

Polym. Mater. 33 (1) (2023) 266–286, https://doi.org/10.1007/s10904-022-02491-x.
[16] Y.M. Al Angari, Magnetic properties of La-substituted NiFe2O4 via egg-white precursor route, J. Magn. Magn Mater. 323 (14) (2011) 1835–1839, https://doi.org/10.1016/j.jmmm.2011.02.003.
[17] J. Setiawan, F.B. Susetyo, D. Nanto, S. Simbolon, H.A. Notonegoro, T. Al Farizi, D. Tihera, Preparation, synthesis and characterizations of La0. 7Sr0. 3Mn (1-y) Ni (y) O3 alloy, Communications in Science and Technology 9 (1) (2024) 87–93, https://doi.org/10.21924/cst.9.1.2024.1361.
[18] H.E. Schaefer, H. Kisker, H. Kronmüller, R. Würschum, Magnetic properties of nanocrystalline nickel, Nanostruct. Mater. 1 (6) (1992) 523–529, https://doi.org/10.1016/0965-9773(92)90085-C.
[19] F.B. Abdallah, A. Benali, M. Triki, E. Dhahri, K. Nomenyo, G. Lerondel, Investigation of structural, morphological, optical and electrical properties of double-doping lanthanum ferrite, J. Mater. Sci. Mater. Electron. 30 (4) (2019) 3349–3358, https://doi.org/10.1007/s10854-018-00608-y.
[20] K.Y.A. Lin, M.T. Yang, J.T. Lin, Y. Du, Cobalt ferrite nanoparticles supported on electrospun carbon fiber as a magnetic heterogeneous catalyst for activating peroxymonosulfate, Chemosphere 208 (2018) 502–511, https://doi.org/10.1016/j.chemosphere.2018.05.127.
[21] O.M. Hemeda, M.Z. Said, M.M. Barakat, Spectral and transport phenomena in Ni ferrite-substituted Gd2O3, J. Magn. Magn Mater. 224 (2) (2001) 132–142, https://doi.org/10.1016/S0304-8853(00)00578-3.
[22] A. Jeidd, M. Amghar, A. Mabrouki, A. Benali, A. Trabelsi, E. Dhahri, B.F.O. Costa, Study of physical properties of the Li 0.5 MgFe 1.5 O 3.5 ferrite nanoparticles, RSC advances 13 (19) (2023) 12906–12916, https://doi.org/10.1039/D2RA07970D.
[23] M.A. Maksoud, A. El-Ghandour, A.H. Ashour, M.M. Atta, S. Abdelhaleem, A.H. El-Hanbaly, A.S. Awed, La3+ doped LiCo0. 25Zn0. 25Fe2O4 spinel ferrite nanocrystals: insights on structural, optical and magnetic properties, J. Rare Earths 39 (1) (2021) 75–82, https://doi.org/10.1016/j.jre.2019.12.017.
[24] M. Hamza, A. ur Rehman, I. Ali, M. Asif, M. Ahmad, Detailed analysis of lanthanum impact on structural, morphological and magnetic properties of manganese spinel ferrites (MnLaxFe2-xO4 x=(0.0, 0.1, 0.2) synthesized through hydrothermal technique, J. Magn. Magn Mater. 564 (2022) 169852, https://doi.org/10.1016/j.jmmm.2022.169852.
[25] A. Manikandan, L.J. Kennedy, M. Bououdina, J.J. Vijaya, Synthesis, optical and magnetic properties of pure and Co-doped ZnFe2O4 nanoparticles by microwave combustion method, J. Magn. Magn Mater. 349 (2014) 249–258, https://doi.org/10.1016/j.jmmm.2013.09.013.
[26] N.R. Dhineshbabu, R. Vettumperumal, A. Narendrakumar, M. Manimala, R. R. Kanna, Optical properties of lanthanum-doped copper spinel ferrites nanoparticles for optoelectronic applications, Adv. Sci. Eng. Med. 9 (5) (2017) 377–383.
[27] B. Nandan, M.C. Bhatnagar, S.C. Kashyap, Cation distribution in nanocrystalline cobalt substituted nickel ferrites: X-ray diffraction and raman spectroscopic investigations, J. Phys. Chem. Solid. 129 (2019) 298–306, https://doi.org/10.1016/j.jpcs.2019.01.017.
[28] M.E. Hajlaoui, S. Gharbi, E. Dhahri, K. Khirouni, Impedance spectroscopy and giant permittivity study of ZnFe2O4 spinel ferrite as a function of frequency and temperature, J. Alloys Compd. 906 (2022) 164361, https://doi.org/10.1016/j.jallcom.2022.164361.
[29] S. Liu, K. Wei, Y. Cheng, S. Yan, L. He, L. Deng, Structural, magnetic and microwave electromagnetic properties in La-substituted quaternary ferrite, J. Alloys Compd. 791 (2019) 469–476, https://doi.org/10.1016/j.jallcom.2019.03.227.
[30] Z.K. Heiba, M.B. Mohamed, M.A. Ahmed, M.A.A. Moussa, H.H. Hamdeh, Cation distribution and dielectric properties of nanocrystalline gallium substituted nickel ferrite, J. Alloys Compd. 586 (2014) 773–781, https://doi.org/10.1016/j.jallcom.2013.10.137.
[31] S. Ikram, J. Jacob, M.I. Arshad, K. Mahmood, A. Ali, N. Sabir, S. Hussain, Tailoring the structural, magnetic and dielectric properties of Ni-Zn-CdFe2O4 spinel ferrites by the substitution of lanthanum ions, Ceram. Int. 45 (3) (2019) 3563–3569, https://doi.org/10.1016/j.ceramint.2018.11.015.
[32] M.N. Akhtar, A.B. Sulong, M.N. Akhtar, M.A. Khan, Systematic study of Ce3+ on the structural and magnetic properties of Cu nanosized ferrites for potential applications, J. Rare Earths 36 (2) (2018) 156–164, https://doi.org/10.1016/j.jre.2017.09.003.
[33] Iqra M.I. Arshad, Z. Munir, N. Amin, M. Akhtar, M.S. Al-Buriahi, A.M. Binzowaimil, M. Al-Hmoud, Enhanced absorption-dominant EMI shielding effectiveness by multi-dimensional Mg0. 33Ca0. 33Cu0. 34Fe2O4/GO nanocomposites under applied magnetic fields, Ceram. Int. (2026), https://doi.org/10.1016/j.ceramint.2026.03.395.
[34] A. Selmi, S. Hcini, H. Rahmouni, A. Omri, M.L. Bouazizi, A. Dhahri, Synthesis, structural and complex impedance spectroscopy studies of Ni0. 4Co0. 4Mg0. 2Fe2O4 spinel ferrite, Phase Transitions 90 (10) (2017) 942–954, https://doi.org/10.1080/01411594.2017.1309403.
[35] M.R. Anantharaman, S. Jagatheesan, K.A. Malini, S. Sindhu, A. Narayanasamy, C. N. Chinnasamy, H.H. Brongersma, On the magnetic properties of ultra-fine zinc ferrites, J. Magn. Magn Mater. 189 (1) (1998) 83–88, https://doi.org/10.1016/S0304-8853(98)00171-1.
[36] H.S. Aziz, S. Rasheed, R.A. Khan, A. Rahim, J. Nisar, S.M. Shah, A.R. Khan, Evaluation of electrical, dielectric and magnetic characteristics of Al–La doped nickel spinel ferrites, RSC advances 6 (8) (2016) 6589–6597, https://doi.org/10.1039/C5RA20981A.
[37] M. Kamran, M. Anis-ur-Rehman, Influence of La3+ substitutions on structural, dielectric and electrical properties of spinel cobalt ferrite, Ceram. Int. 49 (4) (2023) 7017–7029, https://doi.org/10.1016/j.ceramint.2022.10.127.
[38] M. Abdullah-Al-Mamun, M.S.I. Sarker, M.R. Hasan, M.M. Haque, F.A. Khan, M. M. Rahman, M.K.R. Khan, Effect of Er substitution on the magnetic, mössbauer spectroscopy and dielectric properties of CoFe2− xErxO4 (x= 0.00, 0.01, 0.03, 0.05) nanoparticles, Results Phys. 29 (2021) 104698, https://doi.org/10.1016/j.rinp.2021.104698.
[39] M. Naagar, S. Chalia, S. Kharbanda, P. Thakur, A. Thakur, Correlating tailored saturation magnetization of normal-inverse spinels with noncollinear magnetic ordering, J. Mater. Sci. Mater. Electron. 34 (6) (2023) 473, https://doi.org/10.1007/s10854-023-09828-3.
[40] M. Naagar, S. Chalia, P. Thakur, A. Thakur, Effect of lanthanum doping on microstructural, dielectric and magnetic properties of Mn0. 4Zn0. 6Cd0. 2LaxFe1. 8-xO4 (0.0≤ x≤ 0.4), J. Supercond. Nov. Magnetism 34 (10) (2021) 2591–2600, https://doi.org/10.1007/s10948-021-05908-9.
[41] X. Zhou, Y. Zhou, L. Zhou, J. Wei, J. Wu, D. Yao, Effect of Gd and La doping on the structure, optical and magnetic properties of NiZnCo ferrites, Ceram. Int. 45 (5) (2019) 6236–6242, https://doi.org/10.1016/j.ceramint.2018.12.102.
[42] P. Palaniappan, N. Lenin, R. Uvarani, Structural characteristics and electrical properties of lanthanum-doped nanoferrites synthesized by sonochemical method, Appl. Phys. A 128 (9) (2022) 814, https://doi.org/10.1007/s00339-022-05972-5.
[43] S.K. Gore, U.B. Tumberphale, S.S. Jadhav, S.F. Shaikh, A.M. Al-Enizi, A.U.H. S. Rana, R.S. Mane, Grain and grain boundaries influenced magnetic and dielectric properties of lanthanum-doped copper cadmium ferrites, J. Mater. Sci. Mater. Electron. 33 (10) (2022) 7636–7647, https://doi.org/10.1007/s10854-022-07912-8.
[44] K. Praveena, K. Sadhana, Ferromagnetic properties of Zn substituted spinel ferrites for high frequency applications, International Journal of Scientific and Research Publications 5 (4) (2015) 1–21.
[45] F.G. da Silva, J. Depeyrot, A.F. Campos, R. Aquino, D. Fiorani, D. Peddis, Structural and magnetic properties of spinel ferrite nanoparticles, Journal of nanoscience and nanotechnology 19 (8) (2019) 4888–4902, https://doi.org/10.1166/jnn.2019.16877.
[46] S. Aman, M.B. Tahir, N. Ahmad, Retracted article: the enhanced electrical and dielectric properties of cobalt-based spinel ferrites for high-frequency applications, J. Mater. Sci. Mater. Electron. 32 (17) (2021) 22440–22449, https://doi.org/10.1007/s10854-021-06730-8.
[47] S. Gaba, A. Kumar, P.S. Rana, M. Arora, Influence of La3+ ion doping on physical properties of magnesium nanoferrites for microwave absorption application, J. Magn. Magn Mater. 460 (2018) 69–77, https://doi.org/10.1016/j.jmmm.2018.03.035.